JGR Solid Earth

RESEARCH ARTICLE
10.1029/2019JB019076

# Detailed Investigation of the Foreshock Sequence of the 2010 $M_w$7.2 El Mayor-Cucapah Earthquake

**Dongdong Yao[1,2], Yihe Huang[1], Zhigang Peng[2], and Raúl R. Castro[3]**

[1]Earth and Environmental Sciences, College of Literature, Science, and the Arts, University of Michigan, Ann Arbor, MI, USA, [2]School of Earth and Atmospheric Sciences, Georgia Institute of Technology, Atlanta, GA, USA, [3]Centro de Investigación Científica y de la Educación Superior de Ensenada Baja California, Ensenada, Mexico

**Key Points:**
- A waveform matching technique leads to tenfold increase in the number of foreshocks when compared with the SCSN catalog
- We resolve the corner frequency of 20 foreshocks using the detected events as empirical Green's functions
- The relocated catalog and estimated source patches reveal effects of both aseismic slip and cascading stress transfer

**Supporting Information:**
- Supporting Information S1
- Table S1
- Table S2
- Table S3

**Correspondence to:**
D. Yao,
dongdony@umich.edu

**Citation:**
Yao, D., Huang, Y., Peng, Z., & Castro, R. R. (2020). Detailed investigation of the foreshock sequence of the 2010 $M_w$7.2 El Mayor-Cucapah earthquake. *Journal of Geophysical Research: Solid Earth*, *124*, e2019JB019076. https://doi.org/10.1029/e2019JB019076

Received 14 NOV 2019
Accepted 29 APR 2020
Accepted article online 6 MAY 2020

**Abstract** Foreshocks can provide valuable information about possible nucleation process of a mainshock. However, their physical mechanisms are still under debate. In this study, we present a comprehensive analysis of the earthquake sequence preceding the 2010 $M_w$7.2 El Mayor-Cucapah mainshock, including waveform detection of missing smaller events, relative relocation, and source parameter analysis. Based on a template matching method, we find a tenfold increase in the number of earthquakes than reported in the Southern California Seismic Network catalog. The entire sequence exhibits nearly continuous episodes of foreshocks that can be loosely separated into two active clusters. Relocated foreshocks show several seismicity streaks at depth, with a consistently active cluster at depths between 14 and 16 km where the mainshock was nucleated. Stress drop measurements from a spectral ratio approach based on empirical Green's functions show a range between 3.8 and 41.7 MPa with a median of 13.0 MPa and no clear temporal variations. The relocation results, together with the source patches estimated from earthquake corner frequencies, revealed a migration front toward the mainshock hypocenter within last 8 hr and a chain of active burst immediately 6 min prior to the mainshock. Our results support combined effects of aseismic slip and cascading failure on the evolution of foreshocks.

**Plain Language Summary** The 2010 $M_w$7.2 El Mayor-Cucapah (EMC) earthquake was preceded by a prominent sequence of foreshocks starting ~21 days before the mainshock. Several methods based on the similarities of waveforms are applied to obtain spatiotemporal evolution of foreshocks. Ten times more events are found from a template matching method when compared to the SCSN catalog. The refined relative locations reveal two main active clusters in time, as well as two spatial patches with a shallower one to the north of the mainshock epicenter. The depth distribution indicates several linear lines of seismicity, with a consistently active cluster at depths of 14–16 km where mainshock started. An active cluster of foreshocks occurred in the last 6 min. They likely altered the stress state near the hypocenter and ultimately triggered the mainshock. Our analysis indicates that both aseismic slip and cascade triggering processes occurred and contributed to the eventual triggering of the EMC mainshock.

## 1. Introduction

Earthquakes seldom occur by themselves only. Instead, they cluster both in space and time, forming different types of earthquake sequences (e.g., Mogi, 1962). Large earthquakes are followed by a series of aftershocks, and the seismicity rate generally decays with times following the Omori's Law (Omori, 1894; Utsu et al., 1995). Some but not all large earthquakes are also preceded by increasing seismic activity around the mainshock epicenters, known as "foreshocks" (Dodge et al., 1996; Jones & Molnar, 1979; McGuire et al., 2005; Mogi, 1963). The interaction between foreshocks and its role in mainshock nucleation are still unclear (e.g., Gomberg, 2018; Mignan, 2014). In the "nucleation model" or "deterministic model," foreshocks are driven by aseismic deformation as part of a nucleation process that ultimately initiates the mainshock rupture (Bouchon et al., 2011; Dodge et al., 1996; Kato et al., 2012; McGuire et al., 2005). Such an aseismic process has long been suggested by laboratory and numerical modeling studies (e.g., Dieterich, 1979; Ohnaka, 1992) but is only observed or inferred during some earthquake sequences (Bouchon et al., 2011; Kato et al., 2012; Schurr et al., 2014). However, other studies failed to find any evidence for such aseismic process before large mainshocks (e.g., Bakun et al., 2005; Roeloffs, 2006; Wu et al., 2014). In the alternative "cascading model" or "stochastic model," earthquakes trigger each other,

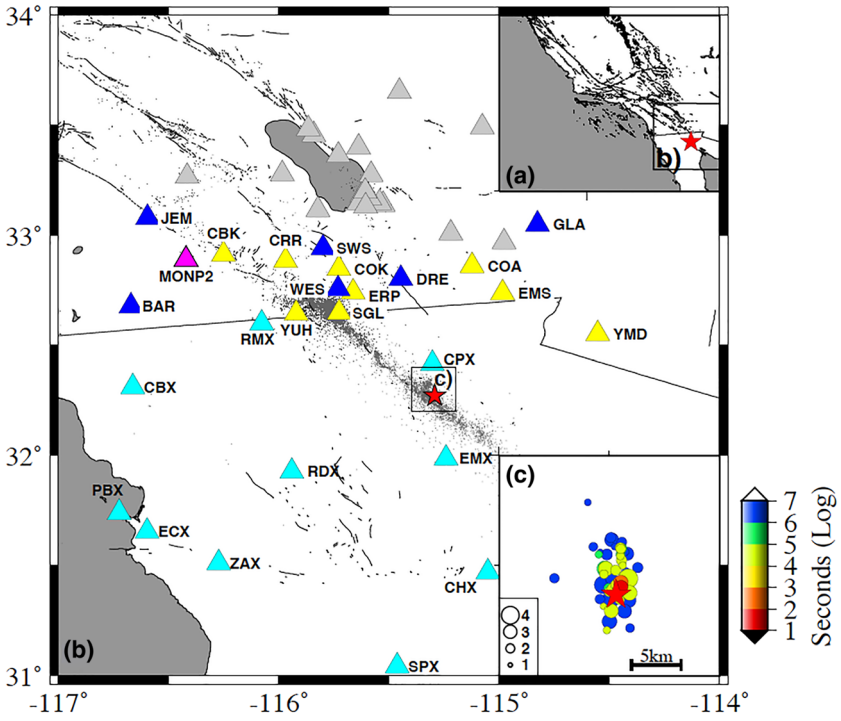


**Figure 1.** Map of the study region. (a) Inset shows the bigger tectonic context, with the 2010 EMC mainshock as the red star. (b) Map shows available seismic stations. Stations in SCSN are shown with blue (network CI and AZ, three-component), yellow (network CI, single vertical component), and gray (unused) triangles. Cyan triangles mark RESNOM stations (network code BC). Background seismicity is shown with gray dots (the updated 1981–2018 catalog file (Hauksson et al., 2012)). (c) A zoomed-in region around the mainshock epicenter (red star). Earthquakes prior to the mainshock are color coded with time relative to the mainshock and scaled with catalog local magnitude.

and the mainshock is simply a triggered event that happens to have a larger size than the last foreshock (Ellsworth & Bulut, 2018; Felzer et al., 2004; Helmstetter et al., 2003). In this case, we would not observe any fundamental difference between a foreshock and an aftershock sequence.

One major challenge in studying foreshock sequences is that the magnitude of completeness ($M_c$) for most foreshock sequences in both regional and global catalogs is relatively high (Mignan, 2014). The underlying spatiotemporal evolution of foreshocks cannot be well established when smaller earthquakes are not adequately detected. Better instrumentation and advanced seismic processing techniques such as template matching methods (Gibbons & Ringdal, 2006; Peng & Zhao, 2009; Shelly et al., 2007) enable us to capture the complete foreshock sequence and constrain its spatiotemporal evolution. This can help to reveal the unique role of foreshocks in mainshock nucleation and test the aforementioned two models (Bouchon et al., 2011; Ellsworth & Bulut, 2018; Kato et al., 2012; Walter et al., 2015; Yoon et al., 2019). More recently, Ross et al. (2019) published a new 10-year catalog in Southern California based on the template matching method, which contains nearly 10 times more events than listed in the standard Southern California Seismic Network (SCSN) catalog. Based on this catalog, Trugman and Ross (2019) reported more pervasive existence of foreshocks that are not detected using the conventional catalogs.

In this study (Figure 1), we revisited the available seismic data set around the 4 April 2010 $M_w$7.2 El Mayor-Cucapah earthquake (thereinafter the EMC mainshock), which ruptured the Mexican Pacific margin in northern Baja California where the Pacific plate moves in the northwest direction relative to the North American plate at a rate of 45 mm/year (Atwater & Stock, 1998; Castro et al., 2011; Wei et al., 2011). We selected this mainshock because it is the largest event around Southern California with a prominent foreshock sequence since the 1999 $M_w$7.1 Hector Mine earthquake (Yoon et al., 2019; Zanzerkia et al., 2003). In addition, it was not included in the recent Quake Template Matching catalog (Ross et al., 2019) since it was located in Northern Mexico outside their study region.

Based on earthquakes listed in the SCSN catalog, Hauksson et al. (2010) relocated both foreshocks and aftershocks of the EMC mainshock. They reported a foreshock sequence that became active about 21 days before the mainshock, occurring within a few kilometers relative to the mainshock epicenter. The local magnitudes of the foreshocks range from 1.5 to 4.4, and the sequence contains two temporal clusters on 21–22 March and 3–4 April (Figure S1 in the supporting information). Chen and Shearer (2013) found that the foreshock sequences of three recent M > 7 earthquakes around Southern California (including the 2010 EMC mainshock) have lower stress drops than background seismicity and aftershocks, suggesting a possible aseismic triggering process. Here we applied various techniques including template matching, magnitude calibration, earthquake relocation, and spectral ratio analysis to obtain a more complete foreshock catalog. We use continuous waveforms in the SCSN for detection and stations in the SCSN and Red Sísmica del Noroeste de México (RESNOM) network (Vidal-Villegas et al., 2018) for relocation. We then used the results to better decipher the spatial-temporal evolution of the foreshock sequence and its role in the nucleation of the EMC mainshock.

## 2. Seismic Data and Analysis Procedures

### 2.1. Earthquake Catalog and Waveform Data

The starting catalog contains earthquakes listed in the Waveform Relocated Earthquake Catalog for Southern California (Hauksson et al., 2012) (the updated 1981–2018 Catalog). We selected events located within the following spatial grid: 115.40 W to 115.20 W, 32.2 N to 32.4 N (Figure 1c and Figure S1). This resulted in a list of 64 earthquakes from 15 March 2010 to the mainshock, distributing along a nearly N-S striking feature (Figure 1c) (Hauksson et al., 2010). SCSN stations within 150 km relative to the mainshock epicenter were selected, including a total number of 16 stations: seven stations with three-component recordings (BH and HH channels with sampling rates of 40 and 100 samples/s) and nine stations with only vertical component (EH channel at a sampling rate of 100 samples/s). Corresponding continuous waveform data were downloaded from the Southern California Earthquake Data Center (SCEDC) using the Seismogram Transfer Program. Specifically, continuous data between 9 March 2010 and 4 April 2010 were requested hourly (using WIN command) for further analysis. Because seismic data recorded by the RESNOM were in triggered mode before the mainshock, they were used only in the relocation stage but not in the event detection process.

### 2.2. Event Detection

We first utilized a matched filter technique (Peng & Zhao, 2009; Walter et al., 2015) to detect as many smaller events as possible during the study window. A 2- to 16-Hz band-pass filter was applied to the continuous data to enhance the signal-to-noise ratio (SNR) for earthquakes within the target region. Sixty-three events listed in the SCSN catalog (excluding the mainshock) were used as templates, and their waveforms were extracted from the filtered continuous data. We started with phase picks requested from SCEDC (with PHASE command) and adjusted them manually via visual inspection. Phase picks with SNR (which is defined as an energy ratio between signal and noise window) above 5 were used, and templates with saved phase from less than three stations were discarded. To save computational cost, only BH channel for three-component stations was used for detection, and data for single-component stations were down-sampled from 100 per second to 40 per second. Then, we utilized a 6-s template window (1 s before and 5 s after the *P* or *S* arrival on vertical/horizontal component, respectively), and computed the waveform cross-correlation (CC) functions for all channels for every hour. We used hourly trace instead of daily trace, because the background noise levels change throughout the day, which would result in differences in the median CC and median absolute deviation values. Hence, using an hourly time window can help to better quantify such fluctuations than using a daily time window. We further shifted the resulting CC functions back to the origin time of template events and stacked them to enhance the detection capability across the network. Only time points corresponding to mean CC values greater than the median CC value of the hourly trace plus 12 times median absolute deviation were considered as positive detections, which ensures low level of spurious detections by random chance (~1% false alarm rate) (Ross et al., 2019). We combined detections from different template events and kept those detections with the highest CC value within half of the template window (Peng & Zhao, 2009). Duplicated events were further removed by cross correlating their corresponding waveforms and keeping the one with the highest CC when two or more detected events have nearly identical

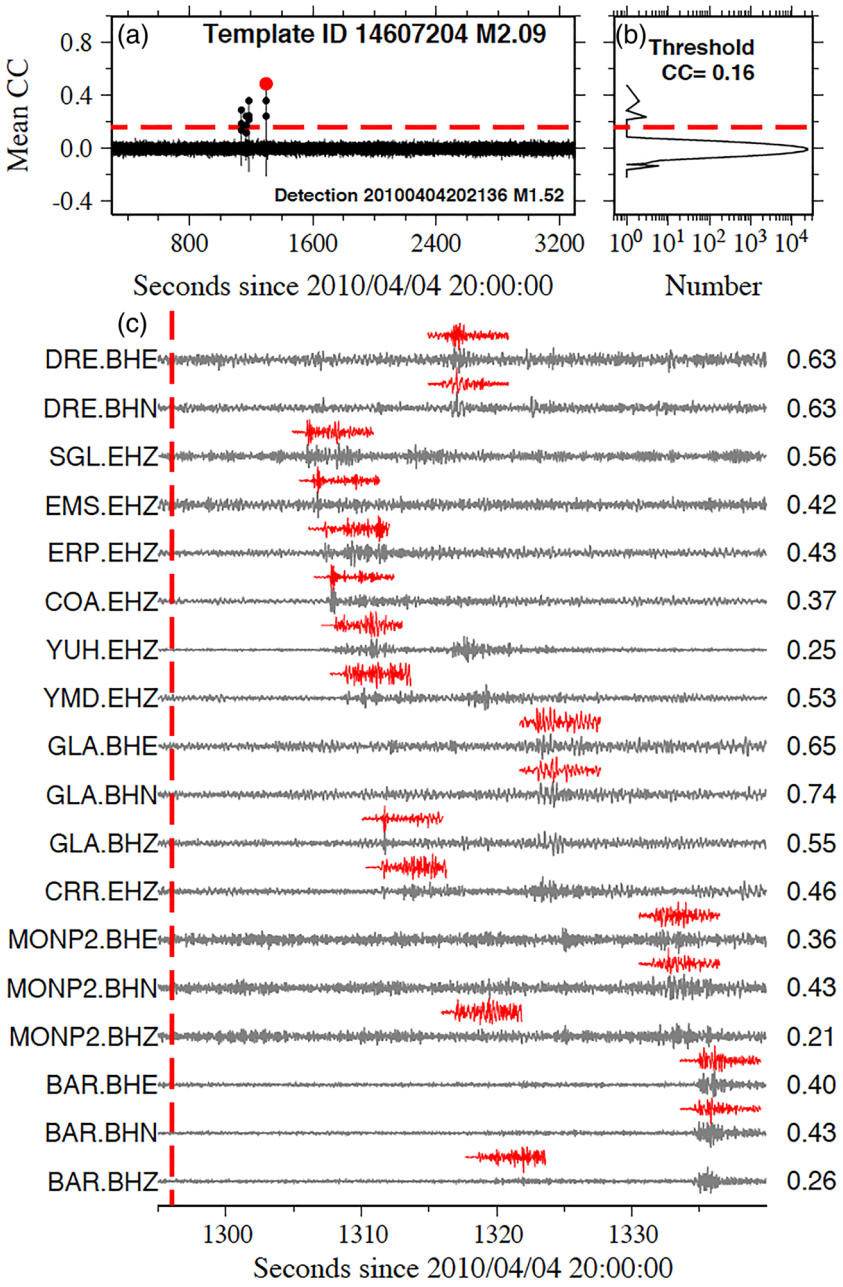


**Figure 2.** An example of a $M_L$1.52 newly detected earthquake (assigned ID: 80404788) from the template 14607204 ($M_L$2.09). (a) Stacked cross-correlation (CC) function around the origin time of the detected event. (b) Histogram of the mean CC values. (c) Waveform comparison between the detected event (gray) and the template (red). STATION.CHANNEL and corresponding CC values are marked on both sides.

waveforms (Figure S2). An example of newly detected event is shown in Figure 2. Using 63 catalog events as templates, we obtained a newly detected catalog containing 666 events (Table S1). We further confirmed they are real earthquakes based on visible *P*/*S* arrivals on certain stations.

### 2.3. Magnitude Calibration

The local magnitude ($M_L$) of a newly detected earthquake was estimated based on the amplitude ratio between the event and its nearby events. Several approaches of amplitude ratio estimation have been used. The peak amplitude ratio measured from peak amplitudes within a small window around *P*/*S* arrivals can be further converted into a local magnitude difference. This widely used approach provides a simple estimation

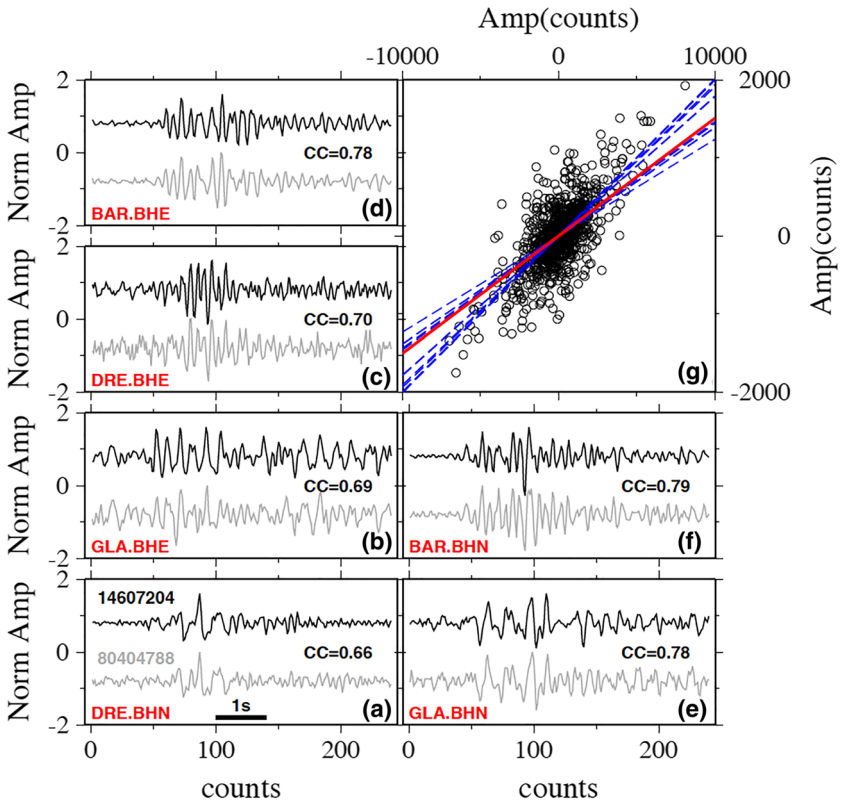


**Figure 3.** Detailed steps for illustrating magnitude calibration. A newly detected event (shown in Figure 2, event ID: 80404788) from template 14,607,204. Panels (a)–(f) show six out of 15 selected channels which are used to compute the amplitude ratio between matched event (gray) and template event (black) waveform (normalized). STATION.CHANNEL and corresponding cross-correlation (CC) coefficients are labeled in each panel. Panel (g) shows matched event amplitude (Y axis) versus template amplitude (X axis). Blue dashed lines mark the first principal component for different station/channel (with values ranging from 0.12 to 0.20), while the red solid line is the median value (0.15), which gives the final amplitude ratio.

of local magnitudes (Huang & Beroza, 2015; Peng & Zhao, 2009; Ross et al., 2018, 2019). Shelly et al. (2016) estimated the amplitude ratios using a principal component fit, which is defined as a data point to data point vector within a template window by aligning the detected event and its matched template waveform. This method stabilizes the amplitude ratio results and provides more robust estimations than the peak amplitude ratios (Meng et al., 2018; Yoon et al., 2019). In this study, we calibrated the local magnitudes by following similar analysis procedures as Meng et al. (2018) with details explained in the methodology part of the supporting information. Figure 3 illustrates the steps to measure the amplitude ratio between a detected event and one matched template. Compared to the peak amplitude ratios, amplitude ratios measured from the principal component fit have less variation across different stations/channels, especially for those with lower CC values (Figure S3).

The newly calibrated local magnitude is set as the median value of measurements from all other matched templates using the following equation:

$$M_L = \text{median}\ (M_{mt} + c^{*}\log_{10}(\text{amplitude ratio})), \quad (1)$$

where $M_{mt}$ is the magnitude for the matched template, and c value depends on the magnitude type and should be 1.0 for local magnitude scale (Shelly et al., 2016). We obtained a similar c value by comparing the amplitude ratio and magnitude difference for template events (Figure S4).

### 2.4. Event Relocation

Event relocation requires accurate *P* and *S* wave differential travel times, which are measured from waveform CC. We first obtained raw waveforms of all events in the detected catalog (120-s waveform: 30 s before to 90 s after the event origin time). We also searched the RESNOM database and extracted waveforms from

trigger-mode stations (Figure 1b). Next, we assigned the phase picks/locations of best-matched catalog events to their detections and manually picked visible phase arrivals for RESNOM stations. We cross-correlated all possible event pairs using a 1.28 s long window around *P* and 2.56 s around *S* waves, starting from 0.32 s before *P* and 0.64 before *S* phase arrivals, respectively. To avoid potential amplitude saturation (clipping) for the mainshock, we matched the mainshock with all foreshocks using a relatively short time window (0.22 s before and 0.08 s after) containing the *P* arrival to measure the differential time after interpolating to 500 Hz, as used in Yoon et al. (2019). Differential travel times were saved when CC is larger than 0.80 for *P* wave and 0.70 for *S* wave. To avoid weakly linked pairs, we required that each pair should have at least four observations. Finally, we utilized the hypoDD algorithm (Waldhauser & Ellsworth, 2000) to relocate events using *P* and S wave differential travel times. Using ~4,520 *P* and ~5,950 *S* differential travel time observations, a total number of 309 events were returned with relative relocations.

### 2.5. Stress Drops and Source Parameters

For an accurate measurement of earthquake rupture dimension and stress drop, we used the spectral ratio method, which can remove common path and site effects of master and empirical Green's function (EGF) event pairs (Abercrombie, 2014, 2015; Hough, 1997; Imanishi & Ellswoth, 2006). In this study, we applied the spectral ratio method to measure stress drops of $M_w$ 2.0–3.5 master earthquakes and quantify their uncertainties. To ensure nearly identical propagating paths, we selected master and EGF event pairs with highly similar waveforms in the foreshock sequence. We cross-correlated events in the detected catalog with each other using a 20 s long window containing both *P* and *S* waves after a 2- to 16-Hz bandpass filtering and chose pairs of master and EGF events with CC coefficients above 0.80 at a minimum of three stations (Abercrombie, 2015; Huang et al., 2016). We also required that the magnitude difference of each event pair is higher than 0.50 and the event pair is recorded by at least three stations. We require the average SNR of *S* wave spectra of EGF events to be higher than 2 for the frequency range of 3–16 Hz. This frequency range was selected based on the expected corner frequencies of target master events. Signal spectra were measured using a 2 s long window starting from manually picked *S* arrivals, while noise spectra were from a 2 s long window immediately before corresponding phases. We also note that the SNRs of *S* waves are generally higher than those of *P* waves for this frequency range (Figure S5).

Individual spectra were computed by taking the Fourier transform of the selected windows of *S* waves. To avoid uneven weighting due to fewer samples in the low frequencies, we interpolated the spectra to a uniform sampling in the logarithmic domain. A multiple window (five 2 s long windows with half window overlapping) and multiple taper (Abercrombie, 2014, 2015; Huang et al., 2016; Prieto et al., 2009) method was applied to enhance the stability of spectral ratios. We fitted the stacked spectral ratio using the Brune (1970) source model to obtain the moment ratio and corner frequency for the master event. Specifically, the nonlinear least squares curve-fitting algorithm in MATLAB (trust-region-reflective optimization) was used, and it returned with optimized values within given search ranges. Similar to Huang et al. (2016), we used a search range with maximum value of 35 Hz for estimated master event's corner frequency ($f_{c1}$). Due to the limited bandwidth of the observation, the corner frequency for the EGF ($f_{c2}$) could be out of the observation range. Since we have no prior information of $f_{c2}$, we set a larger upper limit of 80 Hz (80% of the sampling rate) for its search range. The effect on master event's corner frequency is negligible when this upper limit varies from 35 to 100 Hz (Figure S6). We also measured the median corner frequency of the master event from its multiple EGFs if exist.

## 3. Results

### 3.1. Earthquake Detection and Relocation Results

After obtaining the local magnitudes of all events, we examined the temporal evolution of 666 events in the detected catalog (603 new events + 63 catalog events) (Figure 4a). Many smaller new events with magnitudes between 0 and 2 were identified, showing nearly a continuous sequence (Figure 4). The cumulative frequency-magnitude distribution for catalog foreshocks, detected foreshocks, and catalog aftershocks are shown in Figure S7. We applied the best-combined method (Wiemer, 2001) to compute the magnitude of completeness $M_c$ value for the detected foreshock sequence and then estimated the Guttenberg-Ritcher *b* value using the maximum-likelihood method. The measured *b* value for foreshocks is lower than the value (0.96) of the aftershocks (Hauksson et al., 2010), which is also consistent with what we observed for catalog

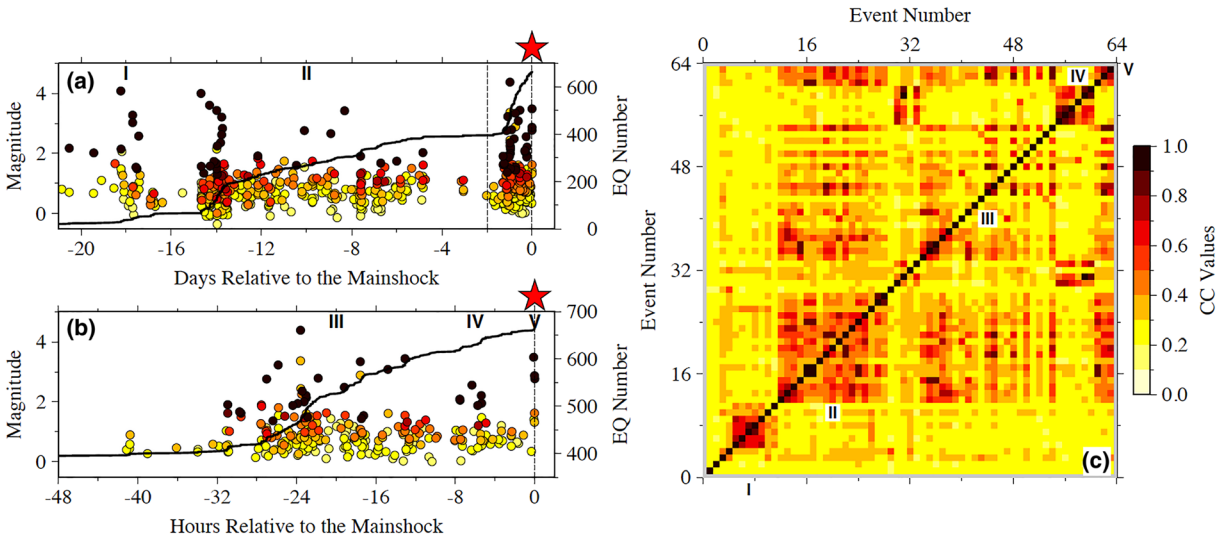


**Figure 4.** Magnitude versus time for events in the detected catalog. (a) Detection result starting 21 days before the mainshock. (b) The detected events within last 2 days prior to the mainshock. Black solid curves in both panels represent the cumulative number of EQ with time. Events are color-coded with the mean cross-correlation (CC) values. (c) Interevent CC matrix. The color bar represents the CC values which falls into [0.0 1.0].

aftershocks with first 120 days (0.80, Figure S7). To verify whether our observation fits into the scenario of varying *b* values for foreshocks and aftershocks (Gulia & Wiemer, 2019), we applied a sliding window to measure *b* value using a constant number of 200 events by considering a time-dependent Mc(t) (Hainzl, 2016). All 666 detected foreshocks were used for the foreshock window, while only ~2,730 catalog aftershocks within first 4 months from the waveform relocated catalog (the updated 1981–2018 catalog) were used for the aftershock period. We observed that the *b* values of foreshocks are lower than those of aftershocks (Figure S8).

The relocated catalog contained 309 events and revealed a complicated sequence of foreshocks, with several bursts of seismicity and multiple streaks of seismicity at different depths (Figures 5 and 6 and Table S2). Two main spatial clusters of seismicity show different depth distributions, and the northern one is shallower when compared to the one surrounding the mainshock epicenter (Figures 5a and 5b). Moreover, the spatio-temporal complexities are also shown in the interevent CC matrix for the 63 catalog events (Figure 4c). Based on their apparent timings, we divided the foreshock sequence into five clusters (Figure 4). In the last 6 min before the mainshock, an intensive sequence containing six events (Cluster V; Figure 7) occurred in regions that were also active during the two major episodes (Clusters II and III). In comparison, the waveforms of Cluster V did not have high similarities with the other two isolated clusters (Clusters I and IV), suggesting that they occurred at different locations. The relocation result for foreshocks with last 48 hr reveals three main streaks of seismicity at depths of 1–5 km, 7–12 km, and 14–16 km (Figure 6b). Due to the poor azimuthal coverage of stations, the absolute locations and depths for these foreshocks may not be well resolved. However, the relative locations between nearby events should be robust, showing that foreshocks occurred only around the mainshock epicenter in the last 8 hr (Figures 5b and 6a).

### 3.2. Stress Drops

Figure 8 shows the spectral ratio results for a master event (SCSN catalog ID: 14607620, $M_w$ 3.49) and three selected EGFs. Similar corner frequencies are resolved from different EGFs for the master event. We obtained the corner frequencies of 20 master events using additional EGF events provided by the newly detected catalog (Figure S9 and Table S3). In order to quantify the uncertainty of master corner frequency, a bootstrapping method was applied to measure the standard error of corner frequency at the 95% confidence level by resampling the residuals 1,000 times (Huang et al., 2016). Note the EGF corner frequency $f_c$ has a large uncertainty due to the limited bandwidth. To measure the seismic moment of each master event, we calibrated the moment magnitude $M_w$ from local magnitude $M_L$ assuming a linear relationship between them:

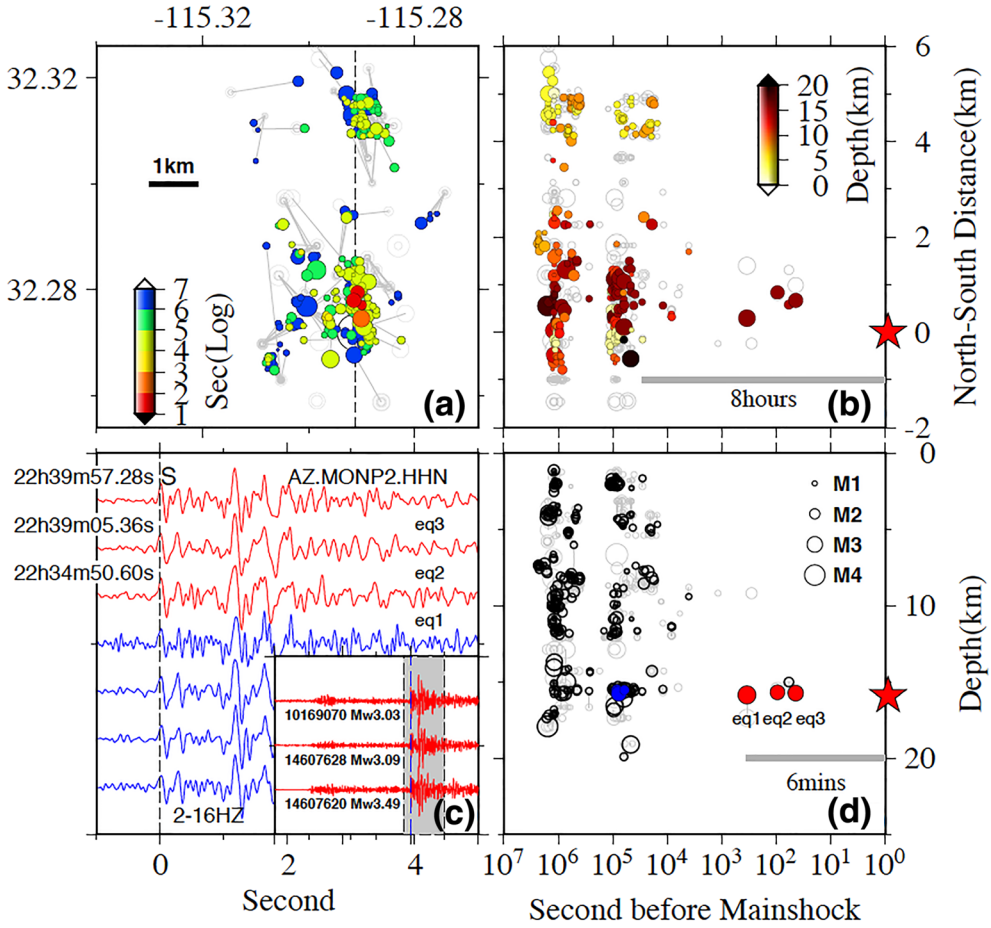


**Figure 5.** (a) Map view of the relocated seismicity. Events are color-coded based on the elapsed time relative to the mainshock. (b) N-S strike distance versus time for relocated seismicity. The color-code is based on depth. (c) Filtered *S* wave (same bandpass filter used in detection/relocation, i.e., 2–16 Hz) recorded by station AZ.MONP2 (Figure 1a) for a few events that occurred at similar depth (see panel (d)). Specifically, three foreshocks within last 6 min (occurrence time is labeled to the left) are shown as red (as indicated in the insert). (d) Depth distribution. Gray circles are events listed in the relocated catalog (1981–2018) (Hauksson et al., 2012).

$$M_w = aM_L + b. \tag{2}$$

Because the moment magnitude is related to the seismic moment as $M_w \sim \frac{2}{3}\log(M_0)$, the seismic moment ratio can be expressed as a function of local magnitude difference between the master event and its EGF:

$$\log_{10}\left(\frac{M_{01}}{M_{02}}\right) = \frac{3}{2}a\Delta M_L. \tag{3}$$

The resulting slope from fitting our measurement was ~1 (Figure S10), corresponding to a value of 2/3 for parameter $a$. We further assumed that the local magnitude converges to moment magnitude with $M_L$ = 3.5 for Southern California (Ross et al., 2016; Shearer et al., 2019) and found the moment magnitudes for all events based on equation 2. Stress drops were then calculated based on a circular crack model (Eshelby, 1957), as shown in the following equation:

$$\Delta\sigma = \frac{7M_0 f_c^3}{16 k^3 v_s^3}. \tag{4}$$

To facilitate comparison with stress drops of earthquakes with similar magnitudes estimated from the same spectral ratio approach (Huang et al., 2016), we assumed $k$ = 0.32 for $S$ wave (Sato &

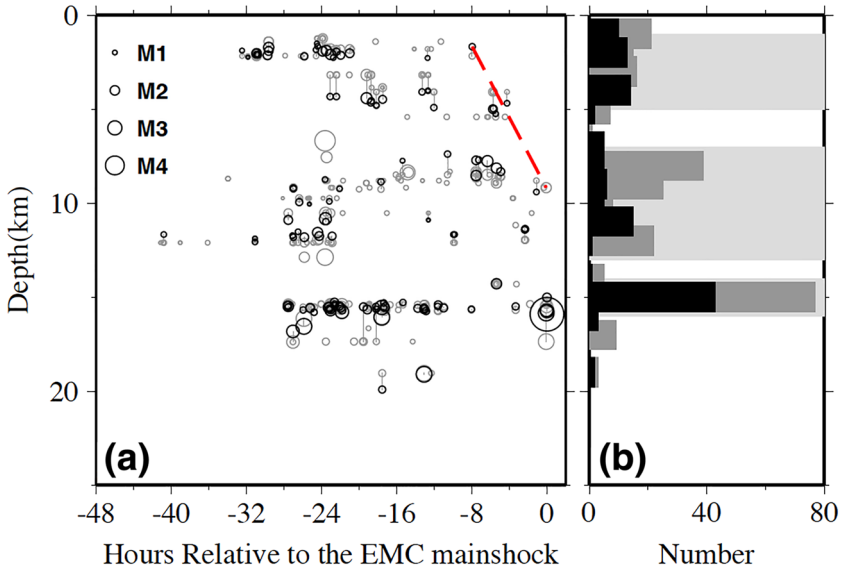


**Figure 6.** (a) Depth versus time with last 2 days prior to the mainshock. Gray and black circles show depths from template catalog (before relocation) and relocated catalog. The red dashed line shows a possible migration front within last 8 hr. (b) Histogram of earthquakes with depth. Shaded areas outline three major streaks.

Hirasawa, 1973), and the averaged *S* wave speed $v_s$ within upper 16 km in this region to be ~3.3 km/s. The S wave stress drops based on the Brune model vary from 3.8 to 41.7 MPa with a median of 13.0 MPa (Figure 8). The stress drops of El Mayor-Cucapah and Guy-Greenbrier earthquakes (Huang et al., 2016) show a very similar range (Figure 8c). We did not observe any temporal change of stress drops of foreshocks before the mainshock (Figure 8d).

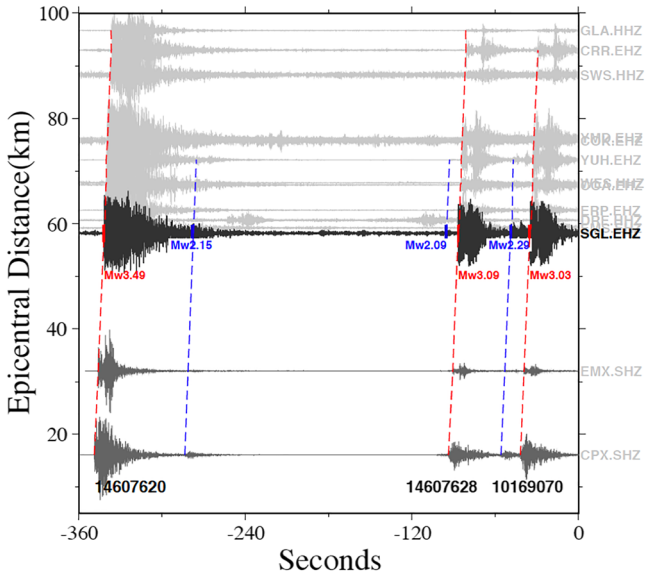


**Figure 7.** Waveforms recorded by stations with distance up to 100 km relative to the cluster within last 6 min (360 s) before the mainshock. Red dashed lines denote three catalog events, while blue dashed lines show newly detected ones. Their corresponding phase arrivals are shown at the closest station in SCSN (CI.SGL). The bottom two waveforms are stations from RESNOM (CPX and EMX).

## 4. Discussion

### 4.1. Comparison With Previous Stress Drop Studies

Our stress drop analysis takes advantage of the highly similar events detected from template matching. The resulting stress drop measurements, given their bootstrapping uncertainties, exhibit a relatively small range, similar to those of potentially induced earthquakes in Guy-Greenbrier sequence in the central United States (Huang et al., 2016). Our stress drop variation may be affected by source geometry and rupture complexity (Huang et al., 2016; Kaneko & Shearer, 2014), since the azimuthal coverage of station distribution is not ideal (Figure 1b). The lower sampling rate (40–50 samples per second) and a lack of continuous recording of RESNOM stations prevent us from including them (with different azimuths) in the detection and stress drop calculation. Other factors that affect the stress drop estimation include the choice of spectral model (Boatwright, 1980; Brune, 1970) and the value of *k* (Brune, 1970; Imanishi et al., 2004; Kaneko & Shearer, 2014; Madariaga, 1976).

Chen and Shearer (2013) concluded that the foreshock sequence within last 2 days preceding the Baja mainshock exhibits a swarm-like behavior. They estimated the stress drops of foreshocks based on the Brune model using an interactive deconvolution and global EGF fitting approach (Shearer et al., 2006). With more smaller foreshocks identified and further used as candidate EGFs, we were able to constrain the stress drop of 20 foreshocks, which is an

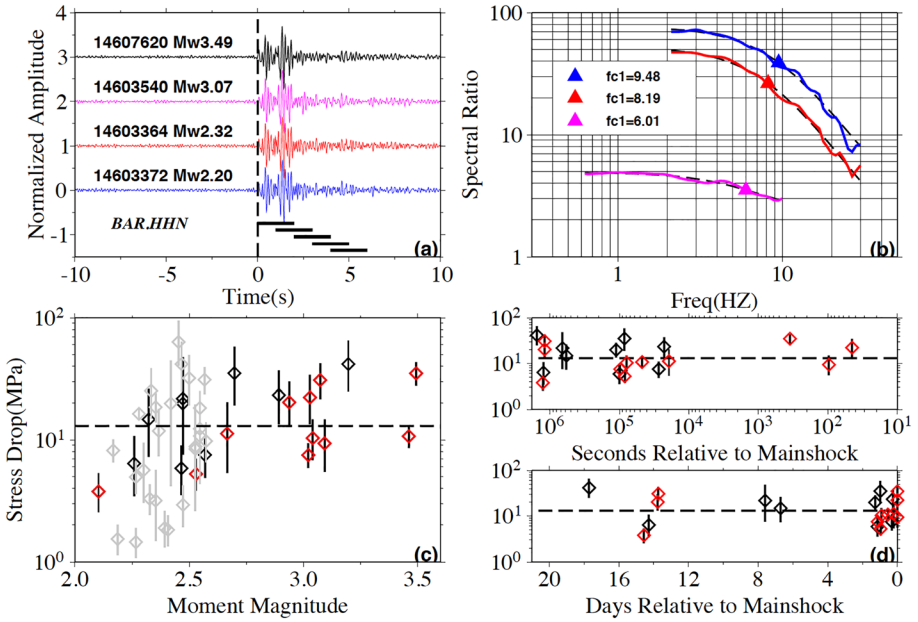


**Figure 8.** Corner frequency measurement for a master event (SCSN event ID: 14607620) and 3 empirical Green's functions (EGFs). Panel (a) demonstrates five consecutive *S* wave windows used to compute the spectral ratios. Panel (b) shows the stacked spectral ratios (solid colored curves) for different EGFs and the fitted curves (black dashed) from the Brune model. The resulting corner frequencies are marked with triangles. (c) Stress drop measurements for all master events in this study (diamonds). Red diamonds indicate median values from multiple EGFs. The error bar gives the stress drop uncertainty at 95% confidence level. Horizontal dashed line shows the median stress drop (13 MPa) for all master evens. In comparison, 25 stress drop estimates for potentially induced earthquakes ($M_w$2.17–2.57) in Guy-Greenbrier sequence are shown with gray diamonds (Huang et al., 2016). (d) The temporal distribution of stress drops both in logarithmic (top) and linear (bottom) time scale.

expansion of the nine foreshocks analyzed previously. The median stress drop estimates obtained from the spectral ratio approach within last 2 days in this study are higher than theirs. One major difference is that our stress drops are estimated from *S* waves, while their stress drops are estimated from *P* waves. We also assume the *k* value of Sato and Hirasawa (1973), whereas Chen and Shearer (2013) used the Madariaga's *k* value. If we use the *k* value of Madariaga (1976) for *S* wave, our median *S* wave stress drop would be even larger than their median *P* wave stress drop. Shearer et al. (2019) analyzed a compact aftershock cluster of the 1992 Landers earthquake and demonstrated a discrepancy of stress drops measurements from different EGF approaches.

Furthermore, biased results could be obtained for the master event's corner frequency ($f_{c1}$) if no constraint is imposed on the smaller EGF event (Shearer et al., 2019). To evaluate the potential effect in our study, we impose fixed values on the corner frequency of the EGF event ($f_{c2}$) by assuming their stress drop is the median stress drop measured from the previous analysis (13 MPa). Then we search for the optimized moment ratio and new $f_{c1}$. Generally, the new $f_{c1}$ is systematically lower than previously resolved $f_{c1}$ (Figure S11, Table S3). We noted that the ratios between previous $f_{c1}$ estimations and new values range from 0.9 to 1.5, and this would lead up to a median factor of 1.6 in the final stress drop estimation. One way to reduce the potential bias of the master event corner frequency is to constrain the corner frequency of the EGF in the spectral ratio analysis. However, this is still challenging for small EGF events whose corner frequencies are usually close to the limit of the sampling band of seismic recordings. In addition, their source spectra are often contaminated by high-frequency noises.

### 4.2. Foreshock Mechanism and Location Uncertainty

We found that the detected foreshocks had complex patterns during the entire sequence. Shallow (less than 12 km) seismicity stopped in the last few hours before the mainshock, resulting in a potential migration of seismicity toward the depth of ~16 km in the middle crust and a cluster of immediate foreshocks right around the eventual mainshock hypocenter (Figure 6a). Hence, the propagating front within last 8 hr implies that aseismic slip may contribute to the foreshock evolution. However, the intensive burst of the

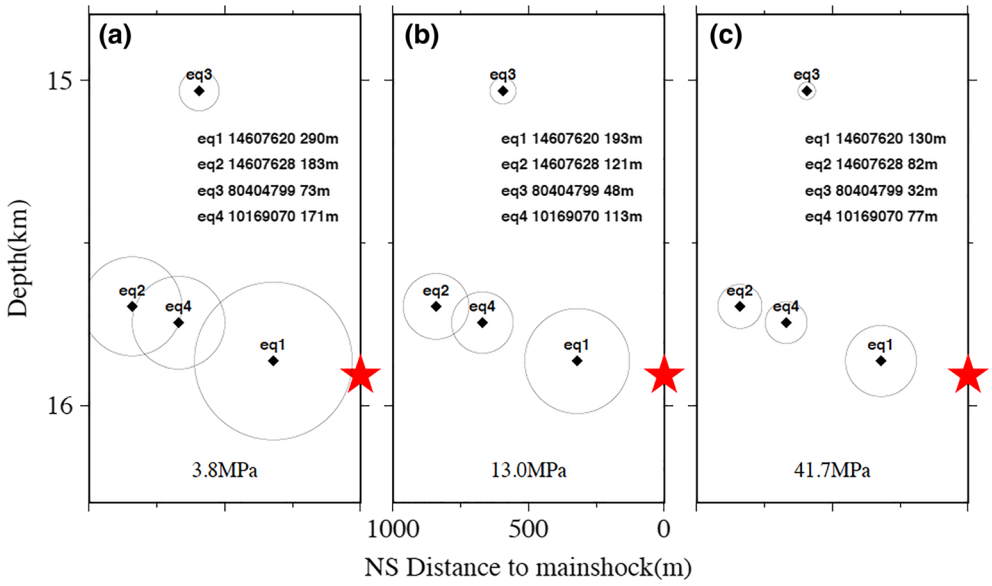


**Figure 9.** Schematic picture shows the distribution of each relocated foreshock within last 6 min. A circular patch and a constant stress drop of minimum 3.8 MPa (a), median 13.0 MPa (b), and maximum 41.7 MPa (c) are assumed to calculate the patch radius. Event IDs and associated radius are labeled on each panel.

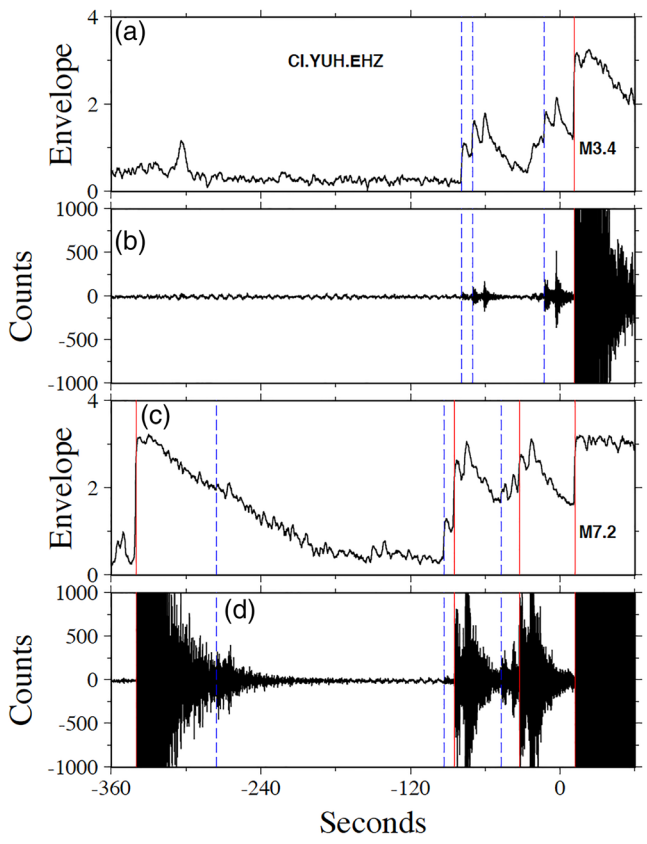


**Figure 10.** Envelope function and waveform recorded by station CI.YUH.EHZ within last 6 min before a $M_L$3.4 foreshock (panels (a) and (b), event ID: 14607412) and the mainshock (panels (c) and (d), event ID: 14607652). Red vertical lines mark events listed in the catalog, while blue dash lines are new detections.

seismicity within last 6 min that occurred close to the hypocentral depth of EMC mainshock (SCSN catalog) may be caused by stress transfer near the mainshock hypocenter. This is because the relative relocations for these immediate foreshocks (Figure 9) showed that their source patches were scattered or partially overlapped, which would fit the cascade triggering model better than the aseismic slip model (e.g., Mignan, 2014), since the latter suggests a preferred migration direction of foreshocks. This interpretation is also consistent with recent observations of the foreshock sequences before the 1999 Izmit and 1999 Hector Mine mainshocks (Ellsworth & Bulut, 2018; Yoon et al., 2019). Finally, Figure S8 shows that the foreshock *b* values are lower than those of aftershocks, which is generally consistent with recent observations in other regions (e.g., Gulia & Wiemer, 2019; Tamaribuchi et al., 2018). However, we only applied template matching to the foreshock sequence, not the aftershock sequence. Hence, one could simply explain such difference in *b* value of the EMC sequence with different types of catalogs, rather than any physical differences before and after the mainshock (e.g., Knopoff et al., 1982).

The source patch size for each foreshock was estimated using a simple circular crack model. Since not all relocated foreshocks within last 6 min have resolvable corner frequency measurement, we used the median stress drop value for the whole foreshock sequence (13 MPa) to compute the source patch radius. We found the epicentral separation is larger than the source patch dimension (Figure 9), which may indicate alternative stress perturbation between different foreshocks other than static stress change. Meanwhile, Fletcher et al. (2010) suggest that the main event actually ruptured along different fault segments, with aftershocks distributed along a different strike when compared with its foreshocks (Hauksson et al., 2010). Better constraints on the hypocentral depth of this foreshock

sequence are also needed to understand its spatial evolution. One solution is to further resolve the absolute locations for larger foreshocks. This requires additional efforts to obtain a better velocity model in this region, which is beyond the scope of this study.

### 4.3. Foreshock of Foreshock

Figure 10 shows the envelope function and waveform within last 6 min prior to both the $M_L$3.4 foreshock (SCSN ID: 14607412; occurrence time: 2010/04/04 09:36:26.74) and the $M_w$7.2 mainshock (SCSN id: 14607652; occurrence time: 2010/04/04 22:40:42.18). Both events were preceded by a sequence of foreshocks with small magnitudes at close locations (Figure S12), while two sequences ended up with "mainshocks" of totally different sizes: The early sequence was followed by the $M_L$3.4 event instead of initiating the mainshock rupture.

One possible explanation is different types of ruptures as suggested by Wen et al. (2018): The earthquakes in the foreshock sequence of the $M_L$3.4 foreshock could be self-arresting ruptures that cannot rupture the whole asperity, while the earthquakes immediately before the mainshock are runaway ruptures and eventually lead up to the mainshock. Alternatively, Yang et al. (2019) proposed that with strong heterogeneity of the stress distribution in the middle crust, the final size of the nucleated event strongly depends on the initiation point, which could be random in space and time. Similarly, Huang (2018) proposed that material heterogenicity such as along-strike segmentation of fault damage zones could influence earthquake size depending on the location of rupture nucleation. Moreover, by examining the early onset of earthquakes with different magnitudes in the Japan subduction zone, Ide (2019) reported nearly identical first rise (~0.2 s) for both small and large earthquakes, indicating that both small and large earthquakes could initiate in the identical way but eventually rupture patches of different sizes. In this case, there is no way to anticipate which one would be the initiation of the eventual mainshock rupture without accurate information of the material properties and stress state surrounding the mainshock patch.

## 5. Conclusion

In this study, we applied various waveform similarity-based techniques to detect and relocate foreshocks of the 2010 $M_w$7.2 EMC mainshock. A total number of 666 earthquakes were found prior to the mainshock. Among all detected foreshocks, 309 events had refined relative relocations, showing two major spatial clusters with one closer to the mainshock epicenter and another shallower one further to the north. Two main temporal clusters were also found, one spanning 21–22 March and another within last 2 days prior to the mainshock. Foreshocks within last 8 hr showed spatial evolution toward the mainshock. An active chain of six foreshocks occurred with last 6 min, and the relative relocations suggested that they might be responsible for triggering the mainshock.

**Acknowledgments**

Seismic data used in this study are requested from Southern California Earthquake Data Center (SCEDC, doi: 10.7909/C32D3xH1) and Ensenada Center for Scientific Research and Higher Education (CICESE, doi: https://doi.org/10.7914/SN/BC, available upon request) and processed with Seismic Analysis Code (SAC) (Helffrich et al., 2013). The operation of the RESNOM network is thanks to the financial support of CONACYT and CICESE. D. Y. and Y. Huang are supported by the University of Michigan, and Z. P. is supported by National Science Foundation (NSF) Grant 1818611. This work is also funded by SCEC Grant 16168. We thank the Associate Editor Satoshi Ide and two reviewers Dr. Blandine Gardonio and Dr. Peter Shearer for their constructive comments to improve the manuscript.

## References

Abercrombie, R. E. (2014). Stress drops of repeating earthquakes on the San Andreas Fault at Parkfield. *Geophysical Research Letters*, *41*, 8784–8791. https://doi.org/10.1002/2014GL062079

Abercrombie, R. E. (2015). Investigating uncertainties in empirical Green's function analysis of earthquake source parameters. *Journal of Geophysical Research: Solid Earth*, *120*, 4263–4277. https://doi.org/10.1002/2015JB011984

Atwater, T., & Stock, J. (1998). Pacific-North America plate tectonics of the Neogene southwestern United States: An update. *International Geology Review*, *40*(5), 375–402. https://doi.org/10.1080/00206819809465216

Bakun, W. H., Aagaard, B., Dost, B., Ellsworth, W. L., Hardebeck, J. L., Harris, R. A., et al. (2005). Implications for prediction and hazard assessment from the 2004 Parkfield earthquake. *Nature*, *437*(7061), 969–974. https://doi.org/10.1038/nature04067

Boatwright, J. (1980). A spectral theory for circular seismic sources: Simple estimates of source dimension, dynamic stress drop, and radiated seismic energy. *Bulletin of the Seismological Society of America*, *70*, 1–28.

Bouchon, M., Karabulut, H., Aktar, M., Ozalaybey, S., Schmittbuhl, J., & Bouin, M. P. (2011). Extended nucleation of the 1999 M-w 7.6. Izmit Earthquake. *Science*, *331*(6019), 877–880.

Brune, J. (1970). Tectonic stress and the spectra of seismic shear waves from earthquakes. *Journal of Geophysical Research*, *75*(26), 4997–5009. https://doi.org/10.1029/JB075i026p04997

Castro, R., Acosta, J., Wong, V., Perez-Vertti, A., Mendoza, A., & Inzunza, L. (2011). Location of aftershocks of the 4 April 2010 Mw 7.2 El Mayor-Cucapah earthquake of Baja California, Mexico. *Bulletin of the Seismological Society of America*, *101*(6), 3072–3080.

Chen, X. W., & Shearer, P. M. (2013). California foreshock sequences suggest aseismic triggering process. *Geophysical Research Letters*, *40*, 2602–2607. https://doi.org/10.1002/grl.50444

Dieterich, J. H. (1979). Modeling of rock friction. 2. Simulation of pre-seismic slip. *Journal of Geophysical Research*, *84*(Nb5), 2169–2175.

Dodge, D. A., Beroza, G. C., & Ellsworth, W. L. (1996). Detailed observations of California foreshock sequences: Implications for the earthquake initiation process. *Journal of Geophysical Research*, *101*(B10), 22,371–22,392. https://doi.org/10.1029/96JB02269

Ellsworth, W. L., & Bulut, F. (2018). Nucleation of the 1999 Izmit earthquake by a triggered cascade of foreshocks. *Nature Geoscience*, *11*(7), 531–535. https://doi.org/10.1038/s41561-018-0145-1

Eshelby, J. D. (1957). The determination of the elastic field of an ellipsoidal inclusion and related problems. *Proceedings of the Royal Society of London, Series A*, *241*, 376–396.

Felzer, K. R., Abercrombie, R. E., & Ekstrom, G. (2004). A common origin for aftershocks, foreshocks, and multiplets. *Bulletin of the Seismological Society of America*, *94*(1), 88–98. https://doi.org/10.1785/0120030069

Fletcher, J., T. Rockwell, O. Teran, E. Masana, G. Faneros, K. Hudnut, et al. (2010), The surface ruptures associated with the El Mayor-Borrego earthquake sequence, *Geological Society of America*, *Cordilleran Section*, Abstract LB1–5, Anaheim, Calif.

Gibbons, S. J., & Ringdal, F. (2006). The detection of low magnitude seismic events using array-based waveform correlation. *Geophysical Journal International*, *165*(1), 149–166. https://doi.org/10.1111/j.1365-246X.2006.02865.x

Gomberg, J. (2018). Unsettled earthquake nucleation. *Nature Geoscience*, *11*(7), 463–464. https://doi.org/10.1038/s41561-018-0149-x

Gulia, L., & Wiemer, S. (2019). Real-time discrimination of earthquake foreshocks and aftershocks. *Nature*, *574*(7777), 193–199. https://doi.org/10.1038/s41586-019-1606-4

Hainzl, S. (2016). Rate dependent incompleteness of earthquake catalogs. *Seismological Research Letters*, *87*(2A), 337–344. https://doi.org/10.1785/0220150211

Hauksson, E., Stock, J., Hutton, K., Yang, W. Z., Vidal-Villegas, J. A., & Kanamori, H. (2010). The 2010 $M_w$ 7.2 El Mayor-Cucapah earthquake sequence, Baja California, Mexico and southernmost California, USA: Active seismotectonics along the Mexican Pacific margin. *Pure and Applied Geophysics*, *168*(8–9), 1255–1277. https://doi.org/10.1007/s00024-010-0209-7

Hauksson, E., Yang, W. Z., & Shearer, P. M. (2012). Waveform relocated earthquake catalog for Southern California (1981 to June 2011). *Bulletin of the Seismological Society of America*, *102*(5), 2239–2244. https://doi.org/10.1785/0120120010

Helffrich, G., Wookey, J., & Bastow, I. (2013). *The Seismic Analysis Code: A Primer and User's Guide* (1st ed.). United Kingdom: Cambridge University Press.

Helmstetter, A., Sornette, D., & Grasso, J. R. (2003). Mainshocks are aftershocks of conditional foreshocks: How do foreshock statistical properties emerge from aftershock laws. *Journal of Geophysical Research*, *108*(B1), 2046. https://doi.org/10.1029/2002JB001991

Hough, S. E. (1997). Empirical Green's function analysis: Taking the next step. *Journal of Geophysical Research*, *102*(B3), 5369–5384. https://doi.org/10.1029/96JB03488

Huang, Y. (2018). Earthquake rupture in fault zones with along-strike material heterogeneity. *Journal of Geophysical Research: Solid Earth*, *123*, 9884–9898. https://doi.org/10.1029/2018JB016354

Huang, Y., & Beroza, G. C. (2015). Temporal variation in the magnitude-frequency distribution during the Guy-Greenbrier earthquake sequence. *Geophysical Research Letters*, *42*, 6639–6646. https://doi.org/10.1002/2015GL065170

Huang, Y., Beroza, G. C., & Ellsworth, W. L. (2016). Stress drop estimates of potentially induced earthquakes in the Guy-Greenbrier sequence. *Journal of Geophysical Research: Solid Earth*, *121*, 6597–6607. https://doi.org/10.1002/2016JB013067

Ide, S. (2019). Frequent observations of identical onsets of large and small earthquakes. *Nature*, *573*(7772), 112–116. https://doi.org/10.1038/s41586-019-1508-5

Imanishi, K., & Ellswoth, W. L. (2006). Source scaling relationships of microearthquakes at Parkfield, CA, determined using the SAFOD pilot hole seismic array. In R. Abercrombie, et al. (Eds.), *Earthquakes: Radiated energy and the physics of faulting*, *Geophys. Monogr. Ser.*, (Vol. 170, pp. 81–90). Washington, D. C: AGU. https://doi.org/10.1029/170GM10

Imanishi, K., Takeo, M., Ellsworth, W. L., Ito, H., Matsuzawa, T., Kuwahara, Y., Iio, Y., Horiuchi, S., & Ohmi, S. (2004). Source parameters and rupture velocities of microearthquakes in Western Nagano, Japan, determined using stopping phases. *Bulletin of the Seismological Society of America*, *94*(5), 1762–1780. https://doi.org/10.1785/012003085

Jones, L. M., & Molnar, P. (1979). Some characteristics of foreshocks and their possible relationship to earthquake prediction and premonitory slip on faults. *Journal of Geophysical Research*, *84*(Nb7), 3596–3608.

Kaneko, Y., & Shearer, P. M. (2014). Seismic source spectra and estimated stress drop from cohesive-zone models of circular subshear rupture. *Geophysical Journal International*, *197*(2), 1002–1015. https://doi.org/10.1093/gji/ggu030

Kato, A., Obara, K., Igarashi, T., Tsuruoka, H., Nakagawa, S., & Hirata, N. (2012). Propagation of slow slip leading up to the 2011 M-w 9.0. Tohoku-Oki earthquake. *Science*, *335*(6069), 705–708. https://doi.org/10.1126/science.1215141

Knopoff, L., Kagan, K. K., & Knopoff, R. (1982). b Values for foreshocks and aftershocks in real and simulated earthquake sequences. *Bulletin of the Seismological Society of America*, *72*(5), 1663–1676.

Madariaga, R. (1976). Dynamics of an expanding circular crack. *Bulletin of the Seismological Society of America*, *66*, 639–666.

McGuire, J. J., Boettcher, M. S., & Jordan, T. H. (2005). Foreshock sequences and short-term earthquake predictability on East Pacific Rise transform faults. *Nature*, *434*(7032), 457–461. https://doi.org/10.1038/nature03377

Meng, X., Yang, H., & Peng, Z. (2018). Foreshocks, b value map, and aftershock triggering for the 2011 $M_w$ 5.7 Virginia earthquake. *Journal of Geophysical Research: Solid Earth*, *123*, 5082–5098. https://doi.org/10.1029/2017JB015136

Mignan, A. (2014). The debate on the prognostic value of earthquake foreshocks: A meta-analysis. *Science Reports-Uk*, *4*.

Mogi, K. (1962). Magnitude frequency relations for elastic shocks accompanying fractures of various materials and some related problems in earthquakes. *Bulletin. Earthquake Research Institute, University of Tokyo*, *40*, 831–853.

Mogi, K. (1963). Some discussions on aftershocks, foreshocks and earthquake swarms: The fracture of a semi-infinite body caused by inner stress origin and its relation to the earthquake phenomena (3rd paper). *Bulletin of the Earthquake Institute*, *41*, 615–658.

Ohnaka, M. (1992). Earthquake source nucleation—A physical model for short-term precursors. *Tectonophysics*, *211*(1–4), 149–178. https://doi.org/10.1016/0040-1951(92)90057-D

Omori, F. (1894). On the aftershocks of earthquakes. *Journal of the College of Science, Imperial University of Tokyo*, *7*, 111–120.

Peng, Z., & Zhao, P. (2009). Migration of early aftershocks following the 2004 Parkfield earthquake. *Nature Geoscience*, *2*(12), 877–881. https://doi.org/10.1038/ngeo697

Prieto, G. A., Parker, R. L., & Vernon, F. L. (2009). A Fortran 90 library for multitaper spectrum analysis. *Comptes Rendus Geoscience*, *35*(8), 1701–1710. https://doi.org/10.1016/j.cageo.2008.06.007

Roeloffs, E. (2006). Evidence for aseismic deformation rate changes prior to earthquakes. *Annual Review of Earth and Planetary Sciences*, *34*(1), 591–627. https://doi.org/10.1146/annurev.earth.34.031405.124947

Ross, Z. E., Ben-Zion, Y., White, M. C., & Vernon, F. L. (2016). Analysis of earthquake body wave spectra for potency and magnitude values: Implications for magnitude scaling relations. *Geophysical Journal International*, *207*(2), 1158–1164. https://doi.org/10.1093/gji/ggw327

Ross, Z. E., Kanamori, H., Hauksson, E., & Aso, N. (2018). Dissipative intraplate faulting during the 2016 Mw 6.2 Tottori, Japan earthquake. *Journal of Geophysical Research: Solid Earth*, *123*, 1631–1642. https://doi.org/10.1002/2017JB015077

Ross, Z. E., Trugman, D. T., Hauksson, E., & Shearer, P. M. (2019). Searching for hidden earthquakes in Southern California. *Science*, *364*(6442), 767–771. https://doi.org/10.1126/science.aaw6888

Sato, T., & Hirasawa, T. (1973). Body wave spectra from propagating shear cracks. *Journal of Physics of the Earth*, *21*(4), 415–431. https://doi.org/10.4294/jpe1952.21.415

Schurr, B., Asch, G., Hainzl, S., Bedford, J., Hoechner, A., Palo, M., et al. (2014). Gradual unlocking of plate boundary controlled initiation of the 2014 Iquique earthquake. *Nature*, *512*(7514), 299–302. https://doi.org/10.1038/nature13681

Shearer, P. M., Abercrombie, R. E., Trugman, D. T., & Wang, W. (2019). Comparing EGF methods for estimating corner frequency and stress drop from P wave spectra. *Journal of Geophysical Research: Solid Earth*, *124*, 3966–3986. https://doi.org/10.1029/2018JB016957

Shearer, P. M., Prieto, G. A., & Hauksson, E. (2006). Comprehensive analysis of earthquake source spectra in southern California. *Journal of Geophysical Research*, *111*, B06303. https://doi.org/10.1029/2005JB003979

Shelly, D. R., Beroza, G., & Ide, S. (2007). Non-volcanic tremor and low-frequency earthquake swarms. *Nature*, *446*(7133), 305–307. https://doi.org/10.1038/nature05666

Shelly, D. R., Ellsworth, W. L., & Hill, D. P. (2016). Fluid-faulting evolution in high definition: Connecting fault structure and frequency-magnitude variations during the 2014 Long Valley caldera, California, earthquake swarm. *Journal of Geophysical Research: Solid Earth*, *121*, 1776–1795. https://doi.org/10.1002/2015jb012719

Tamaribuchi, K., Yagi, Y., Enescu, B., & Hirano, S. (2018). Characteristics of foreshock activity inferred from the JMA earthquake catalog. *Earth, Planets and Space*, *70*. https://doi.org/10.1186/s40623-018-0866-9

Trugman, D. T., & Ross, Z. E. (2019). Pervasive foreshock activity across southern California. *Geophysical Research Letters*, *46*, 8772–8781. https://doi.org/10.1029/2019GL083725

Utsu, T., Ogata, Y., & Matsuura, R. (1995). The centenary of the Omori formula for a decay law of aftershock activity. *Journal of Physics of the Earth*, *43*(1), 1–33. https://doi.org/10.4294/jpe1952.43.1

Vidal-Villegas, J. A., Munguia, L., Gonzalez-Ortega, A., Nuñez-Leal, M. A., Ramirez, E., Mendoza, L., et al. (2018). The northwestern Mexico seismic network: real time seismic monitoring in north Baja California and northwestern Sonora, Mexico. *Seismological Research Letters*, *89*(2A). https://doi.org/10.1785/0220170183

Waldhauser, F., & Ellsworth, W. L. (2000). A double-difference earthquake location algorithm: Method and application to the northern Hayward Fault, California. *Bulletin of the Seismological Society of America*, *90*(6), 1353–1368. https://doi.org/10.1785/0120000006

Walter, J. I., Meng, X., Peng, Z., Schwartz, S. Y., Newman, A. V., & Protti, M. (2015). Far-field triggering of foreshocks near the nucleation zone of the 5 September 2012 (Mw 7.6) Nicoya Peninsula, Costa Rica earthquake. *Earth and Planetary Science Letters*, *431*, 75–86.

Wei, S., Fielding, E., Leprince, S., Sladen, A., Avouac, J. P., Helmberger, D., et al. (2011). Superficial simplicity of the 2010 El Mayor-Cucapah earthquake of Baja California in Mexico. *Nature Geoscience*, *4*(9), 615–618. https://doi.org/10.1038/ngeo1213

Wen, J., Chen, X., & Xu, J. (2018). A Dynamic Explanation for the Ruptures of Repeating Earthquakes on the San Andreas Fault at Parkfield. *Geophysical Research Letters*, *45*, 11,116–11,122. https://doi.org/10.1029/2018GL079140

Wiemer, S. (2001). A software package to analyse seismicity: ZMAP. *Seismological Research Letters*, *72*(3), 373–382. https://doi.org/10.1785/gssrl.72.3.373

Wu, C., Meng, X., Peng, Z., & Ben-Zion, Y. (2014). Lack of spatiotemporal localization of foreshocks before the 1999 Mw 7.1 Duzce, Turkey, earthquake. *Bulletin of the Seismological Society of America*, *104*(1), 560–566. https://doi.org/10.1785/0120130140

Yang, H., Yao, S., He, B., Newman, A. V., & Weng, H. (2019). Deriving rupture scenarios from interseismic locking distributions along the subduction megathrust. *Journal of Geophysical Research: Solid Earth*, *124*, 10,376–10,392. https://doi.org/10.1029/2019JB017541

Yoon, C. E., Yoshimitsu, N., Ellsworth, W. L., & Beroza, G. C. (2019). Foreshocks and mainshock nucleation of the 1999 Mw7.1 Hector Mine, California, earthquake. *Journal of Geophysical Research: Solid Earth*, *124*, 1569–1582. https://doi.org/10.1029/2018JB016383

Zanzerkia, E. E., Beroza, G. C., & Vidale, J. E. (2003). Waveform analysis of the 1999 Hector Mine foreshock sequence. *Geophysical Research Letters*, *30*(8), 1429. https://doi.org/10.1029/2002GL016383